IMMUNOLOGY

Stiff matrix impairs cytotoxic T lymphocyte function at multiple levels

Mir Hadi Seyedzadeh[1]†, M. A. Kristine Tolentino[2]†, Newton Gil Peres[1], Eric Y. Du[2], Florence Bartlett-Tomasetig[3], Gaia M. N. Javier[4], Kristopher A. Kilian[2,5], Katharina Gaus[1]‡, Jesse Goyette[1]*, J. Justin Gooding[2]*

Cytotoxic T lymphocytes (CTLs) play a pivotal role in antitumor immunity via inducing apoptosis in cancer cells. However, their effector functions can be compromised by the perturbations in the tumor microenvironment (TME). Among the diverse factors within the TME, the effects of stiffness of the extracellular matrix (ECM) on CTL-mediated responses require greater understanding. To address this gap, we three-dimensionally bioprinted CTLs and targeted cells in polyethylene glycol–based ECM mimics with tunable stiffness and uniform porosity. Our findings reveal that CTLs in stiffer ECMs showed reduced migration speed and impaired antigen-specific cytotoxicity. Synapse formation analysis revealed that stiffer ECMs impair CTL efficacy not by reducing the frequency of CTL-target cell contacts but by shortening the contact time between these cells, a consequence of disrupted immunological synapse formation. Live Ca^{2+} imaging and expression of phospho-ZAP70 confirmed these findings. Together, these results suggest that ECM stiffness modulates CTL function at multiple levels, from migration to cytotoxicity and synapse quality.

INTRODUCTION

Cytotoxic T lymphocytes (CTLs) migrate through tissues searching for transformed or virally infected cells. Using the T cell receptor (TCR), CTLs scan and search for target cells, and, upon recognizing the specific peptide antigen and major histocompatibility complex–I (pMHC), they undergo reorganization of their cytoskeleton and form cytolytic synapses with target cells. Subsequently, the CTLs release granules containing perforin and granzymes as well as cytokines into the synapse that eventually induce apoptosis in target cells (*1*, *2*). These cytotoxic interactions conclude when CTLs detach from their current targets and move on to engage with other nearby cells (*3*, *4*).

Antitumor CTL-killing responses are modulated by several suppressive factors within the tumor microenvironment (TME), including aspects of an altered extracellular matrix (ECM). Generally, solid tumors are characterized by a markedly increased ECM stiffness relative to healthy tissues (*5*, *6*), which can act as a barrier limiting the access of T cells to the core of the tumor (*7*–*9*). Immune cell infiltration into tumor sites is directly correlated with favorable prognosis in several types of solid tumors (*10*–*12*). Notably, one reason T cell–based therapies have shown promising outcomes in certain blood malignancies is the lack of a dense TME (*13*, *14*). Fibrotic responses to tumor growth can lead to alteration in ECM mechanics, more specifically, an increased matrix stiffness. Increased ECM stiffness also favors tumor progression by various mechanisms, including promoting an aggressive phenotype of tumor cells and promoting invasion (*15*). Lowering the stiffness of the ECM enhances T cell migration and boosts the effectiveness of immunotherapy in tumors (*16*–*18*). Biomechanical cues modulate the activation, migration, phenotype, and function of T cells through mechanosensitive ion channels and integrins, which translate biomechanical signals to downstream signaling pathways (*19*, *20*).

To understand the complex role of TME components, three-dimensional (3D) culture systems have been of growing interest as conventional 2D monolayer cell cultures do not replicate TME complexities (*21*). While natural hydrogels, such as collagen and Matrigel, are widely used as scaffolds for 3D culture studies, they have limitations with regards to batch-to-batch variability and potential xenogeneic contaminants (*22*). Synthetic hydrogels, particularly, polyethylene glycol (PEG), bridge the gap to these limitations. Furthermore, these hydrogels yield a broader range of stiffness and allow a precise control of bioactive cues through bioconjugation reactions (*23*–*25*). Previously, PEG-based hydrogels were used to mimic the condition of ECM in lymph nodes to increase ex vivo T cell proliferation (*26*). Building on the advances in technology and material science, 3D bioprinting further overcomes the challenges associated with natural hydrogels and enhances the utility of PEG in tissue engineering applications. This innovative technique has shown promising outcomes in the 3D reconstruction of complex biological structures such as the TME (*27*). Consistent spatial organization, precise control over the physical properties of the matrix, and rapid high-content analysis can be achieved using 3D bioprinting (*28*). Bioprinting of T cells is a relatively new approach to studying T cells ex vivo (*29*). A few studies have focused on T cell activation by generating artificial antigen-presenting cells (APCs) or imitating lymph nodes and lymphatic vessels (*30*–*32*). Nevertheless, the fate of embedded T cells in 3D hydrogel and the subsequent effects of the ECM mimics on their effector function are not well described. In particular, stiffness in the TME varies because of the changes in the mechanical properties of the ECM, yet the extent to which T cells are prone to these physical nuances remains unclear.

Here, we aimed to investigate the effects of matrix stiffness on antigen-specific CTL-killing function in a well-defined 3D culture

[1]Department of Molecular Medicine, School of Biomedical Sciences, Faculty of Medicine and Health, University of New South Wales Sydney, Sydney, Australia. [2]School of Chemistry and Australian Centre for NanoMedicine, University of New South Wales Sydney, Sydney, Australia. [3]Katharina Gaus Light Microscopy Facility, Mark Wainwright Analytical Centre, University of New South Wales Sydney, Sydney, Australia. [4]School of Photovoltaic and Renewable Energy Engineering, University of New South Wales Sydney, Sydney, Australia. [5]School of Materials Science and Engineering, University of New South Wales Sydney, Sydney, Australia.
*Corresponding author. Email: justin.gooding@unsw.edu.au (J.J.G.); j.goyette@unsw.edu.au (J.G.)
†These authors contributed equally to this work.
‡Deceased.

platform. We used chemical strategies to tune the stiffness without compromising the concentration of biochemical cues and porosity. Furthermore, we seek to mimic the stiffness of soft tissues where CTLs are predominantly found. We used the RASTRUM 3D bioprinter and bioinks to create a 3D hydrogel embedded with CTLs and target cells. By optimizing a 3D bioprinter-based killing model, we investigated how variation in matrix stiffness influences CTL function, including migration, target search-and-kill behavior, and synapse formation. While we monitored Ca^{2+} flux as an indirect readout of T cell activation, we also quantified phosphorylated zeta-chain–associated protein kinase 70 (phospho-ZAP70) as a metric for TCR-proximal signaling.

RESULTS

Soft and stiff PEG-based hydrogels with embedded viable cells were fabricated via 3D bioprinting

We have previously shown that manually prepared PEG-based hydrogels can be used as ECM mimics for CTLs (*33*). To set up a 3D bioprinted T cell killing assay, we utilized the RASTRUM 3D bioprinter and its bioink system, which embeds cells into the PEG-based ECM-mimetic hydrogels (*28*, *34*). These hydrogels comprised two key components: (i) a four-arm PEG maleimide bioink and (ii) a bisthiol cross-linker. Upon printing, the maleimide from the bioink and the thiol from the cross-linker trigger a rapid gelation via the Michael addition reaction (Fig. 1, A and B) (*33*, *34*). We tuned the matrix stiffness by varying the molecular weight of the bioink (10 or 20 kDa) and cross-linking it with the cross-linker, ensuring a consistent 1:2 maleimide-to-thiol ratio. When the bioinks were cross-linked, the resultant hydrogels exhibited stiffness values of 0.7 kPa for 20-kDa bioink and 1.5 kPa for 10-kDa bioink (Fig. 1C) without varying the microporosity (Fig. 1D) as evaluated by cryo–scanning electron microscopy (fig. S1). This result is consistent with our previous comprehensive porosity characterization of the same and other similar PEG hydrogels (*35*, *36*). This chemical strategy enabled us to generate hydrogels with a controlled, twofold difference in stiffness, allowing us to systematically investigate the impact of matrix stiffness on CTL function. Furthermore, these inert hydrogels do not contain bioactive cues that could influence CTL migration or cytotoxic function, enabling us to isolate stiffness as the only biophysical variable.

To evaluate CTL function within these ECM mimetic hydrogels, we utilized an OT-1 T cell killing assay with antigen expressing Chinese hamster ovary (CHO) cells as the APC. Following ex vivo activation, splenocytes isolated from OT-1 mice were enriched for $CD8^+$ T cells capable of recognizing and responding to target cells presenting ovalbumin (OVA)–H2Kb as the pMHC (fig. S2). We used CHO T-Rex cells treated overnight with doxycycline (10 ng/ml) as OVA^+ or cognate target cells and wild-type CHO cells as OVA^- or noncognate target cells (fig. S3A). These cells stably expressed pMHC for 24 hours at similar levels as cells that were treated continuously with doxycycline (fig. S3B).

The bioprinter used a sterile bioprinting cartridge, into which bioinks and cross-linkers containing cells are added (*34*). To prevent premature CTL-target cell interactions during bioprinting, target cells were combined with bioinks, whereas CTLs were mixed with the cross-linker. Directly mixing both cell types into either the bioink or the cross-linker would result in a premature killing occurring in a 2D context rather than the intended killing within a 3D environment. For each condition, these mixtures were loaded separately into the bioprinter and printed into 96-well plates, followed by adding culture medium after 5 min. This procedure is illustrated in Fig. 1E.

A reliable killing assay requires that the cell viabilities are comparable. Thus, we aimed to identify the time window postprinting at which viability of CTLs and target cells is comparable. To assess the impact of bioprinting on cell viability, we imaged live and dead cells at various time points postprinting. CTLs were bioprinted either with medium as a non-3D control or within ECM mimetic hydrogels as 3D test samples. A comparable CTL viability, regardless of stiffness, was observed 1 and 24 hours postprinting. A slight reduction in viability was observed in stiff ECM mimic compared with soft ECM mimic after 48 hours (Fig. 1F). To simulate the conditions of the killing assay, target cells were mixed with bioinks and printed with cell-free cross-linkers. In the control condition, target cells were printed directly into medium without cross-linkers. Viability assays revealed no significant difference between soft and stiff ECM mimics, with target cell viability remaining high up to 48 hours postprinting (Fig. 1G). These results indicate that the first 24 hours postprinting represent an optimal window for coculture and cytotoxicity assays as bioprinting had minimal impact on cell viability within this timeframe.

CTL search-and-kill function was negatively affected in stiff ECM mimics

T cell motility is critical for locating target cells and delivering cytotoxic effects (*37*). To characterize the migration of CTLs in soft and stiff bioprinted ECM mimics, we tracked the movement of fluorescently labeled CTLs within the ECM mimics in the absence and presence of target cells for 1 hour via time-lapse imaging. Whether target cells are absent or present, CTLs migrate faster in soft ECM mimic compared with stiff ECM mimic (Fig. 2A). This result aligns with previous studies on ECM mimics with different compositions that also showed faster migration of CTLs in softer ECMs (*16*, *33*, *38*). Additional CTL migratory metrics—such as straightness, displacement, and total distance travelled in 3D—also indicated faster migration in the soft ECM mimic (fig. S4, E to G). When OVA^+ target cells were introduced, the speed of CTLs significantly slowed down in both soft and stiff ECM mimics (Fig. 2A), as illustrated in fig. S4 (A to D). This behavior was expected as CTLs arrest migration after encountering target cells that express cognate antigens as shown in movies S1 and S2 (*37*).

Because CTLs can migrate within these ECM mimics, they should be able to search for target cells, a prequel for killing. Next, we investigated whether, upon locating their targets, CTLs could effectively kill them. To assess this, we measured the killing efficiency of CTLs against OVA^+ target cells in both soft and stiff ECM mimics. An endpoint cytotoxicity assay was performed using 3D imaging to quantify the number of dead target cells. To identify the target cells from CTLs in coculture, CTLs and target cells were labeled with CellTracker Deep Red and CellTrace Violet, respectively. Cell viability was then assessed using the dead-cell marker ethidium homodimer-1. Killing efficiency was calculated on the basis of the difference in viability of OVA^+ target cells in the presence of CTLs between their viability in the absence of CTLs. Notably, CTLs exhibited higher cytotoxicity in soft ECM mimic, with a greater number of dead OVA^+ target cells compared with those in stiff ECM mimic (Fig. 2, B and C).

Subsequently, we investigated whether these CTL killings events were antigen-specific or not. To achieve that, we determined the antigen-specific killing efficiency where both OVA^+ and OVA^- target cells were cocultured with CTLs. Each effector-to-target (E:T) ratio

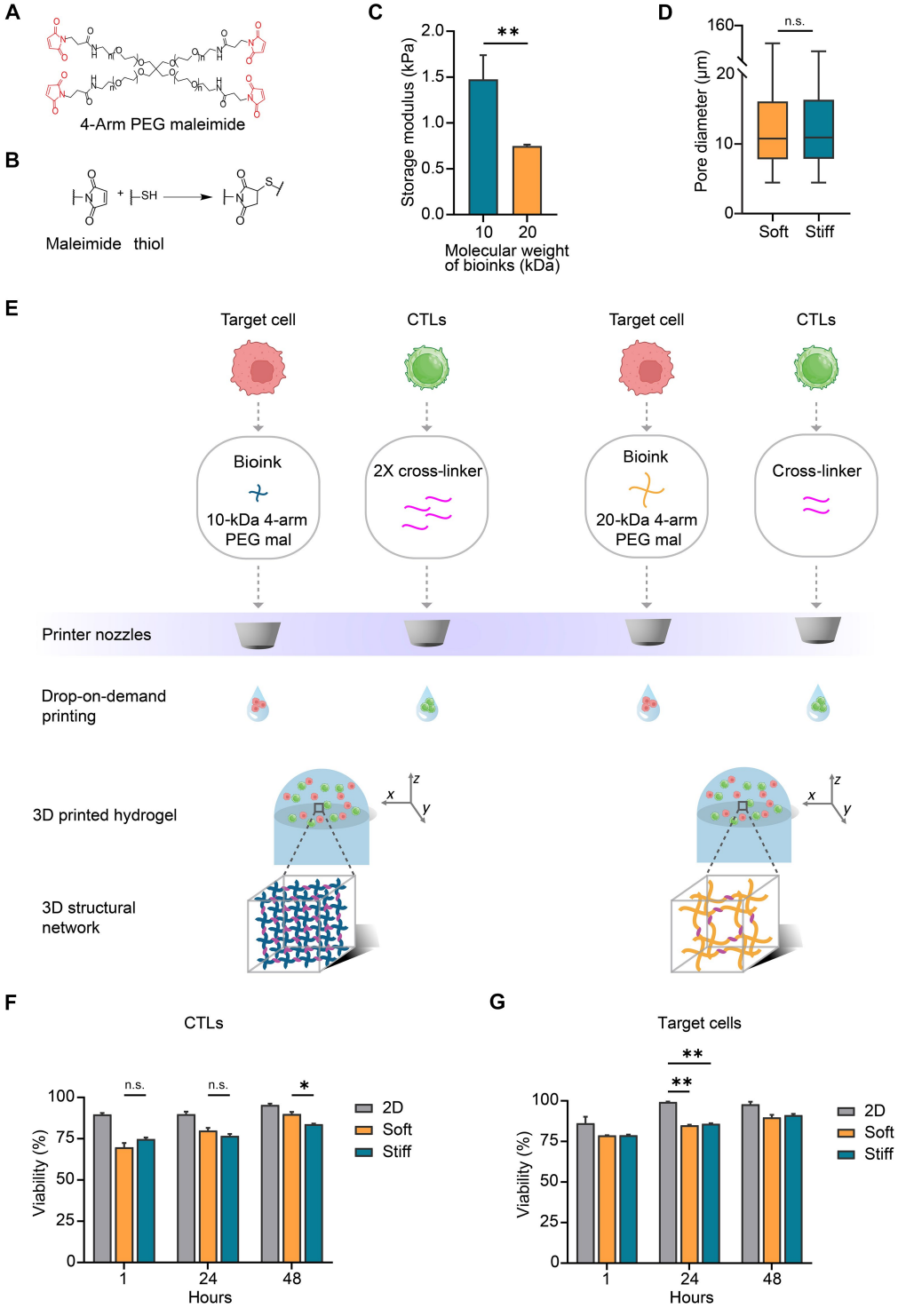

Fig. 1. Viable cells were bioprinted with soft and stiff PEG-based ECM mimics. (**A**) The chemical structure of four-arm PEG maleimide (bioink) is shown, with cross-linking functional groups highlighted in red. (**B**) The Michael addition reaction between maleimide groups (of four-arm PEG maleimide) and thiol groups (of the cross-linker) served as the cross-linking mechanism to form the hydrogels. (**C**) Stiffness values of cell-free, 3D bioprinted hydrogels were measured within the linear viscoelastic region at 1 Hz and 0.1% strain ($n = 3$). Data represent the means + SD. Statistical analysis was performed using a *t* test. (**D**) Pore size measurement of the soft and stiff hydrogels. Data are presented as box plots, with whiskers representing the minimum and maximum values, and were statistically analyzed with the Mann-Whitney test. (**E**) Schematic representation of the 3D bioprinting process of the soft and stiff bioinks with embedded cells. T cells were combined with cross-linkers, whereas target cells were incorporated into the bioinks, resulting in their encapsulation within soft and stiff hydrogels. mal, maleimide. Viability of (**F**) CTLs and (**G**) OVA^+ target cells in medium (2D), soft hydrogels (0.7 kPa), and stiff hydrogels (1.5 kPa) was assessed over time using 3D confocal imaging and LIVE/DEAD assay. Statistical testing by two-way analysis of variance (ANOVA). Data represent the means ± SEM. n.s., $P \geq 0.05$; *$P < 0.05$; **$P < 0.01$. Created in BioRender. J. Gooding (2025), https://BioRender.com/97vb7z2.

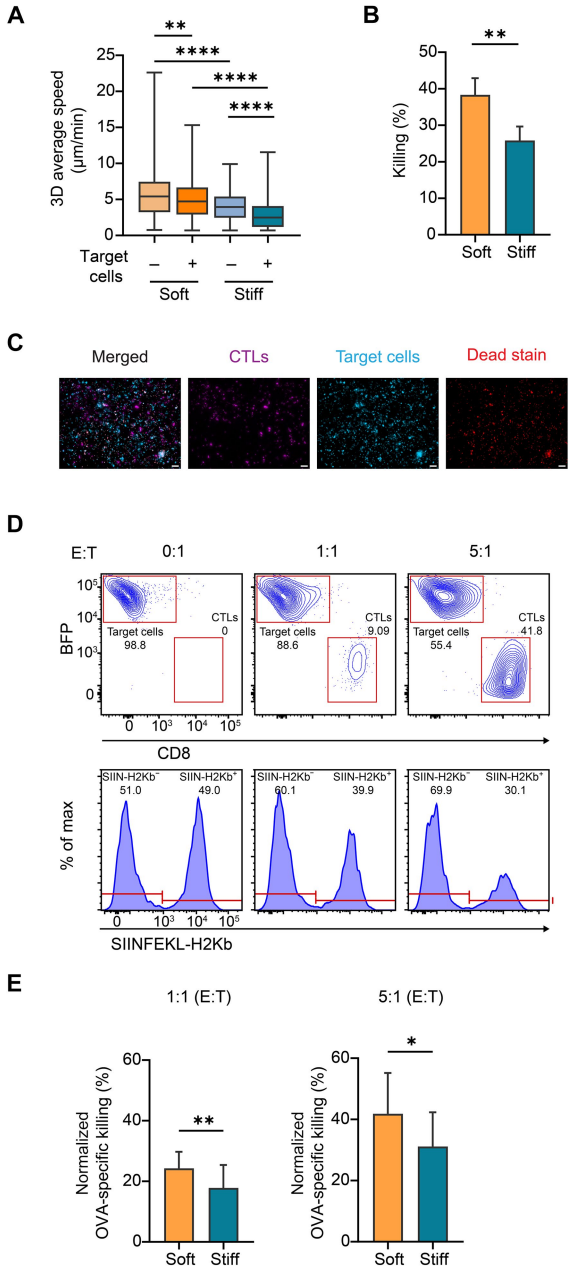

Fig. 2. Stiffer ECM mimic impaired CTLs search-and-kill function. (**A**) CTL migration speed was reduced in stiff ECM mimic. CTL migration was tracked for 1 hour in the absence and presence of target cells in PEG hydrogels. Data are presented as a box plot, with whiskers representing the minimum and maximum values, and were statistically analyzed via the Kruskal-Wallis test. (**B**) CTL killing was impaired in stiff ECM mimic. CTLs were bioprinted with OVA^+ target cells in either soft or stiff ECM mimic ($n = 4$). The number of dead target cells was quantified with ethidium homodimer-1 and normalized to target cell controls (without CTLs). Data are presented as means ± SD and analyzed using *t* test. (**C**) Representative images of CTL-killing OVA^+ target cells in ECM-mimetic hydrogel (0.7-kPa PEG) 24 hours postprinting. CTLs and target cells were labeled with CellTracker Deep Red and CellTrace Violet, respectively. Ethidium homodimer-1 was used to determine cell death. (**D**) Representative flow cytometry plots and histograms of the 3D bioprinted killing assay. OVA^+ and OVA^- target cells were cobioprinted into soft and stiff ECM-mimetic hydrogels with CTLs at effector-to-target (E:T) ratios of 0:1, 1:1, and 5:1. (**E**) Antigen-specific killing efficiency at 1:1 and 5:1 E:T ratios. Data were normalized to 0:1 E:T, presented as means ± SD ($n = 4$), and analyzed using the Mann-Whitney test. *$P < 0.05$; **$P < 0.01$; ****$P < 0.0001$.

was determined on the basis of the number of CTLs relative to equal numbers of OVA^+ and OVA^- target cells. The flow cytometry–based assay was first optimized in the conventional (2D) culture (fig. S3, C to E). For the 3D assay, at each E:T ratio, equal numbers of OVA^+ and OVA^- target cells were mixed with either 0.7- or 1.5-kPa bioinks. Meanwhile, the number of CTLs in the cross-linkers was adjusted to achieve the desired E:T ratio. After 20 to 24 hours, CTLs with both cognate and noncognate target cells were recovered from the bioprinted ECM mimics and stained for surface markers. Gating strategies are shown in Fig. 2D. The decrease in the second peak in Fig. 2D indicates that CTLs were able to recognize and kill the cognate target cell even in the presence of noncognate target cells in culture, thus supporting an antigen-specific killing. Furthermore, at a 1:1 E:T ratio, CTLs demonstrated significantly higher killing efficiency in soft ECM mimic compared with stiff ECM mimic, consistent with our result in Fig. 2B. We did not observe bystander killing in our system as the number of OVA^- target cells in cocultures remained unchanged in both soft and stiff matrices (fig. S3F). Increasing the E:T ratio to 5:1 consequently enhanced the killing efficiency in both soft and stiff ECM mimics, with the soft ECM mimic consistently promoted a higher CTL-mediated killing than the stiff ECM mimic (Fig. 2E). Notably, changes in stiffness did not affect antigen presentation and stiffness of the target cells, as analyzed under the 0:1 E:T condition (fig. S3, G to I), further supporting that the difference in antigen-specific killing is due to the difference in the ability of CTLs to kill in environment with different stiffness.

Expression of T cell activation markers correlates strongly with their cytotoxic function, representing the downstream effects of signaling and phenotypic modulation. When we tested expression of surface activation markers CD69 and CD25, as well as the inhibitory receptor PD1, in CTLs recovered from hydrogels, we observed cognate-antigen dependent response increases and significantly lower expression in cells recovered from stiff gels, indicating less activation (fig. S5, A to C). In contrast, production of interferon-γ and tumor necrosis factor–α was similar from T cells in soft and stiff hydrogels, suggesting that this function was less sensitive to ECM stiffness (fig. S5, D and E). We also validated that cells retained effector phenotype (>97% $CD44^{hi}$/$CD62L^{lo}$) in all conditions (fig. S5F).

Decreased killing efficiency in stiff ECM mimic was due to shorter contact time between CTLs and target cells

To investigate the mechanisms underlying the reduced CTL-killing efficiency in stiff ECM mimic, we examined the dynamics of the killing process, including conjugate formation, target cell death, and release of the target cell (*39*). Following the same setup for the killing assay, fluorescently labeled CTLs and target cells were bioprinted into soft and stiff ECM mimics and incubated for 24 hours. Subsequently, the samples were imaged every 10 min over 12 hours. This approach enabled us to monitor individual contact events or conjugates, conduct a multistep analysis of the CTL effector function, and correlate these findings with the endpoint assays presented in the previous section. Representative images in Fig. 3A show several steps involved in the killing process: conjugate formation, death of target cell, and released of the target cell. From these images, metrics such as the number of conjugates, contact time, and time of release were extracted and quantified.

Antigen presentation and killing requires formation of an immunological synapse. A plausible explanation for reduced killing efficiency in stiffer gels is the impaired ability of CTLs to form conjugates with

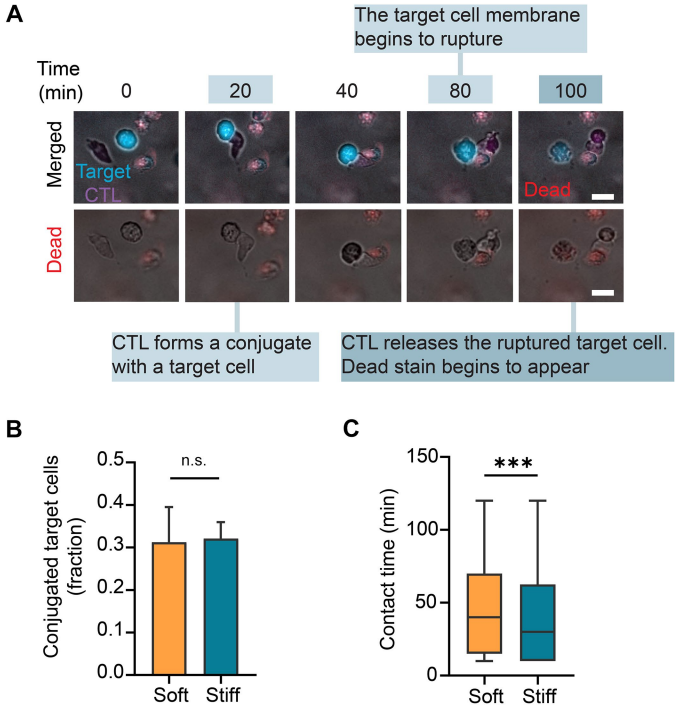

Fig. 3. CTLs had longer contact time with target cells in soft than in stiff ECM mimic. (**A**) Representative time-lapse images of a 3D bioprinted killing assay depicting the interaction between CTLs and target cells. CTLs, stained with CellTracker Deep Red (violet), formed conjugates with target cells stained with CellTrace Violet (cyan), leading to membrane rupture in the target cells as indicated by the uptake of the dead cell marker ethidium homodimer-1 (scale bars, 20 μm). Time-lapse images were captured every 10 min for 12 hours, starting 24 hours postbioprinting. (**B**) Quantitative analysis of the fraction of target cells that formed conjugates with CTLs, presented as means ± SD. Statistical significance was assessed using a *t* test. (**C**) Time of contact between CTLs and target cells. Data are presented as a box plot, with whiskers representing the minimum and maximum values, and were statistically analyzed with the Mann-Whitney test. n.s., $P \geq 0.05$; ***$P < 0.001$.

target cells. We expected this to manifest as the difference in the number of conjugates formed between CTLs and target cells in soft and stiff matrixes. To test our hypothesis, we counted the number of conjugates formed between CTLs and target cells with a custom-built code. The data analysis flowchart is available in fig. S6. We calculated the 3D distance between CTLs and target cells, with any distance of 12 μm and below was recognized as a conjugate. This threshold was based on the average sum of radii of a CTL and a target cell. A unique combination of CTL and target cell was counted as one conjugate. Thus, conjugates from the same CTL and target cell that persist over time are only counted once, which prevented overcounting of conjugates. We normalized the unique number of conjugates to the total unique number of cells in the sample to account for the difference in cell count between samples. Contrary to our initial hypothesis, this analysis revealed that the fraction of target cells conjugated with CTLs over the course of the imaging was similar between the soft and stiff ECM mimics (Fig. 3B). This implies that CTLs can still find and form conjugates with target cells in stiff ECM mimic despite migrating slower than CTLs in soft ECM mimic (Fig. 2B). Because CTLs could kill more efficiently in soft than in stiff ECM mimic as established in Fig. 2 (B and E), these findings also indicated that not all conjugates formed between CTLs and target cells resulted in killing. Time-resolved data from microscopy experiments are also consistent with these findings, showing that more conjugates are formed than dying target cells over time. Consistent with the endpoint killing data in Fig. 2 (B and E), the percentage of dead target cells relative to the number of conjugates in soft is higher than in stiff, indicating higher killing efficiency (fig. S7). Overall, this finding implies that ECM stiffness affects the efficiency of antigen-specific activation at CTL-target synapses and subsequent effector functions in CTLs.

We then wondered whether the stiffness of the ECM mimics influences synapse stability, which could explain the difference in killing efficiency between soft and stiff ECM mimics. We propose that the stability of synapse can be probed by the duration of contact between a CTL and a target cell, referred to as contact time. Using the algorithm that identified the conjugates, we also extracted the time when the conjugate was formed and the time when the target cell was released. These events were identified as the earliest and latest time points when a unique conjugate was detected. Contact time was then calculated as the difference between the time of release and the time of conjugation. With this, we found that CTLs formed significantly longer contact time with target cells in soft ECM mimics compared with stiffer ECM mimics (Fig. 3C). This suggests that soft ECM mimics promote more stable or efficient immune synapse formation, which may enhance the CTL-killing effector function.

CTLs form less efficient synapses in stiff ECM mimic

The shorter contact times associated with stiff ECM mimic suggests a poor synapse quality. A likely reason is a defect in TCR signaling. To investigate this, we measured the Ca^{2+} influx in CTLs, which occurs upon TCR-pMHC recognition or T cell activation (*40*, *41*). Furthermore, perturbations in the TME can impair CTL effector functions by dysregulating Ca^{2+} channels, thereby limiting serial killing (*3*). Thus, Ca^{2+} influx serves as a key indicator of effective or impaired TCR-proximal signaling (Fig. 4A).

To probe how matrix stiffness affects synapse quality, we used the Ca^{2+} indicator Fluo-4 AM to monitor Ca^{2+} signaling in CTLs (*3*, *40*, *41*). Following the bioprinting of CTLs with cognate target cells in soft and stiff ECM mimics, we loaded the cells with Ca^{2+} indicator and imaged them every 30 s for 1 hour. Figure 4B shows representative images demonstrating that the Ca^{2+} indicator fluoresced when a CTL formed a synapse with its cognate target cell. This Ca^{2+} influx indicates that an effective immunological synapse was formed between the CTL and the target cell, triggering a cascade of signaling events that ultimately lead to apoptosis of the target cell (*42*).

Next, we quantified the Ca^{2+} influx in CTLs conjugated with target cells. The CTL-target cell conjugates were identified through the same algorithm described in the previous section (fig. S6). Determining the presence of Ca^{2+} influx in CTLs could be challenging due to the transient, fading, and intermittent nature of the indicator. To identify the presence of Ca^{2+} influx in CTLs, we analyzed the intensity picked up by the conjugated CTLs in the green (Ca^{2+} indicator) channel. A representative bimodal intensity distribution is shown in Fig. 4C. The first peak with lower intensity values refers to the background, whereas the second peak with higher intensity values refer to the positive signal from Ca^{2+} indicator in CTLs. To computationally determine the threshold intensity value that separates these two peaks, we applied an image processing algorithm known as the Otsu's thresholding. The Otsu's thresholding algorithm analyzes the intensity histogram of an image and automatically finds the best cutoff intensity to separate objects from the background by minimizing

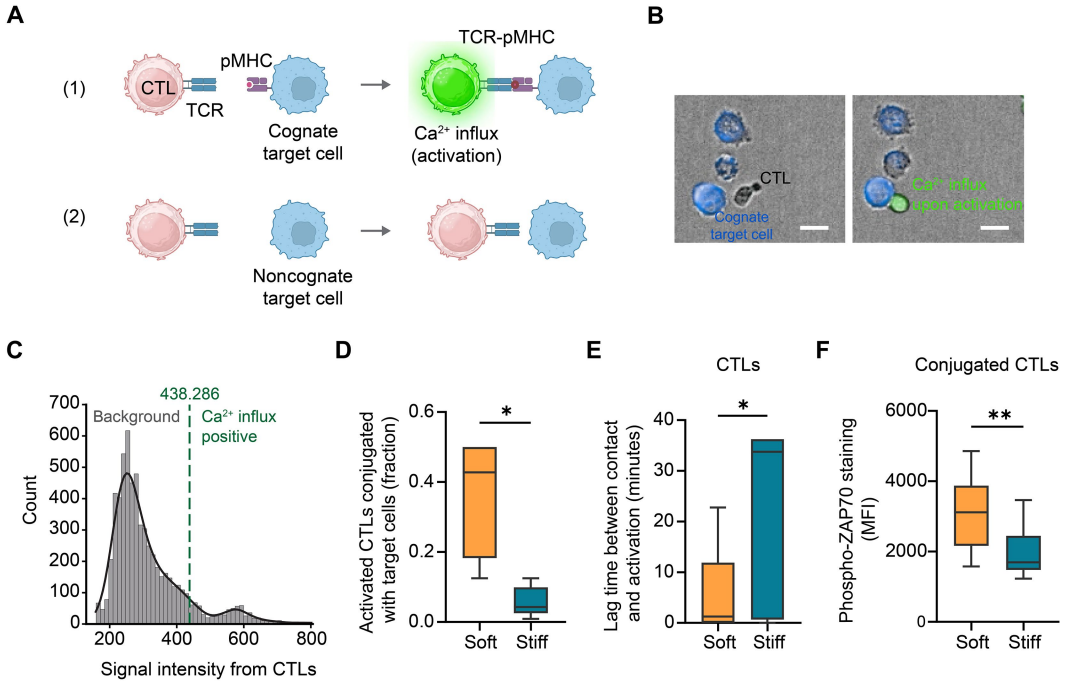

Fig. 4. Synapse efficiency dampened in the stiff ECM mimic. (**A**) Schematic illustration of Ca^{2+} influx in CTLs and target cells: (1) In the presence of OVA-H2Kb, TCR-pMHC recognition leads to CTL activation and Ca^{2+} influx in CTLs. (2) In the absence of OVA-H2Kb, CTL activation is not observed. (**B**) Representative images of Ca^{2+} influx in a CTL upon activation by a cognate target cell. Scale bars, 10 μm. (**C**) Representative fluorescence intensity histogram of CTLs in green (Ca^{2+} indicator) channel to identify and measure the Ca^{2+} influx in conjugated CTLs. The threshold intensity depicted in green dashed line was identified by Otsu's thresholding algorithm. (**D**) The fraction of CTL-target cell conjugates that resulted in T cell activation. (**E**) Lag time of CTL activation. (**F**) Phospho-ZAP70 levels in CTLs conjugated with target cells measured as mean fluorescence intensity (MFI) of anti–phospho-ZAP70 staining. Data are presented as box plots, with whiskers representing the minimum and maximum values, and were statistically analyzed with the Mann-Whitney test. *$P < 0.05$; **$P < 0.01$. Created in BioRender. J. Gooding (2025), https://BioRender.com/i6flttt.

intraclass variance (*43*). We applied the thresholding algorithm to each time point to account for the transient, fading, and intermittent nature of Ca^{2+} indicator (fig. S8). Any conjugated CTL with intensity value above the threshold was considered activated. Our analysis revealed that, among the CTL-target cell conjugates, soft ECM mimic facilitates more T cell activation than stiff ECM mimic (Fig. 4D). This indicates that the stiffness of the matrix affects the synapse quality, with soft ECM mimic promoting efficient synapse than stiff ECM mimic.

Another metric that can quantify the synapse quality is the delay of the Ca^{2+} influx in the conjugated CTLs. Using the algorithms that identified conjugate formation and detected Ca^{2+} influx, we determined the time when these events occur. The lag time was calculated as the difference between synapse formation and Ca^{2+} influx. This analysis shows a significant delay in T cell activation in the stiff ECM mimic (Fig. 4E).

Decreased Ca^{2+} signaling in response to cognate antigen suggests a defect in TCR signaling. To more directly test this, we next examined the TCR-proximal signaling by quantifying phospho-ZAP70 in CTLs conjugated with target cells. Consistent with diminished TCR activation, conjugated CTLs in the stiff matrix exhibit lower phospho-ZAP70 expression than those in the soft matrix (Fig. 4F and fig. S9). Together, these results further corroborate that stiff ECM mimic impaired synapse quality.

DISCUSSION

CTLs are key effector cells in eliminating antigen-specific target cells in viral infections and tumors. However, the extent to which matrix stiffness in a 3D environment influences CTL function still needs better understanding. Here, we leveraged the RASTRUM 3D bioprinting platform to develop and validate a robust cytotoxicity assay using mouse OT-1 CTLs and antigen-specific target cells. By using a synthetic and tunable PEG-based hydrogel, we precisely controlled the matrix stiffness to investigate its effects on CTL function. Previous studies on 3D T cell cultures primarily relied on natural and hybrid hydrogels, such as alginate (*44*), hyaluronic acid (*45*), collagen (*46*), and Matrigel (*47*) where they primarily emphasized and established T cell activation and proliferation. Building upon this foundation, our work extends to evaluating the effector function within synthetic ECM mimics.

Previous studies have demonstrated that the RASTRUM 3D bioprinter, in conjunction with four-arm PEG maleimide bioinks, enables rapid gelation, modular design, and compatibility with various cancer cell lines (*34*). Our earlier work extended the use of these PEG-based hydrogels as ECM mimic to CTLs, providing a 3D structural support that promotes cell viability and migration (*33*). Building on these capabilities, we show how CTL killing is modulated by matrix stiffness independent of other bioactive cues. Our ECM mimics achieved a physiologically relevant stiffness range (0.7 to 1.5 kPa) that capture the mechanical properties of soft tissues where CTLs are predominantly active such as secondary lymphoid tissues and lungs (*45*, *48*) while maintaining similar porosity (*35*). This property is consistent with a similar PEG-based hydrogels (*36*). In most cases, matrix stiffness and porosity are entwined in both natural and synthetic materials (*38*).

One limitation of using certain hydrogels as ECM mimics for CTLs is the difficulty in retrieving cells embedded within the matrix. The limitation is particularly notable, as flow cytometry–based assays, widely used to understand CTL function, requires single-cell suspension. Here, our 3D bioprinted ECM mimic with embedded CTL-target cocultures were easily digested via proteolysis using the Cell Retrieval Solution, allowing for efficient cell recovery and generating a single-cell suspension for downstream analysis. This gel digestion is comparable to collagen-based assays, where T cells were cultured and recovered (*38*). By leveraging this cell retrieval capability, we utilized flow cytometry to probe antigen-specific CTL killing in our ECM mimics, corroborating the findings from the microscopy-based killing assay.

With these advancements, we explored fundamental biological questions about CTL function within a 3D environment. Our findings reveal that ECM stiffness, independent of other bioactive cues, plays a key role in CTL migration and killing. Specifically, we observed that stiffer ECM mimics reduced CTL motility and CTL-mediated killing, aligning with previous reports showing slower CTL migration and decreased CTL-mediated killing in dense collagen matrices (*8*, *38*). Furthermore, increasing CTL density increased antigen-specific killing, consistent with previous 3D in vitro and in vivo studies (*39*, *49*). Notably, introducing OVA^+ target cells to CTL cultures slowed CTL migration in both soft and stiff ECM mimics. This supports the expected behavior of CTLs upon encountering cognate target cells, where they survey the surface of the target cell and establish an immunological synapse, resulting in slower migration speed, as evidenced in Fig. 3A and fig. S4 (A to D). While past studies could not distinguish whether these suppressive effects were driven independently by collagen concentration, differences in pore size, or matrix stiffness, our work provides a clearer insight into the direct influence of matrix stiffness on CTL dynamics.

Subsequently, we dived deeper to understand why CTLs were less effective at killing target cells in stiff ECM mimics. At first, we hypothesized that the slower migration in stiffer environment simply inhibits the frequency of CTL-target cell interaction. However, our time-lapse assay revealed that the number of CTL-target cell conjugates was similar in both soft and stiff ECM mimics, suggesting that the difference is not due to a decreased ability of CTLs to find and form contacts with target cells in stiff ECM mimics. This observation contrasts with a previous report that less conjugates formed in stiffer than softer collagen-based matrices (*38*). In that study, conjugate formation was assessed at a single time point after an hour of encapsulation, which may have limited the opportunity for the slower-migrating cells to locate their targets. Our approach was to extend this observation window to allow sufficient time for CTLs in both soft and stiff ECM mimics to migrate and find target cells: We monitored conjugate formation over a 12-hour period following 24 hours of encapsulation. This extended observation period provides a more comprehensive understanding of CTL-target interactions.

While the similar count of conjugates between soft and stiff ECM mimic does not explain the difference in killing efficiency, this observation suggests that not all conjugates formed between a CTL and a target cell result in successful killing. This led us to wonder whether the stiffness of the environment influenced the synapse quality formed between CTLs and target cells, which could explain the difference in killing efficiency in soft and stiff ECM mimic. Previous studies have demonstrated that matrix stiffness influences synapse formation, with softer matrices promoting $CD8^+$ T cell activation more effectively than stiffer ones (*45*, *46*). Consequently, we probed the synapse quality using three metrics: (i) contact time between CTLs and target cells, (ii) Ca^{2+} flux, and (iii) phospho-ZAP70 intensity in conjugated CTLs.

We observed that the contact time between a CTL and a target cell was shorter in stiff than in soft ECM mimic, indicating less stable synapse formation in the stiffer environment. A shorter contact time may limit perforin delivery to target cells, potentially allowing them to recover and resulting to lower killing efficiency in the stiffer environment (*39*). Furthermore, a shorter contact time may provide insufficient opportunity to complete the TCR-pMHC formation, potentially impairing target cell recognition. We tested this hypothesis by measuring T cell activation using Ca^{2+} flux assay. Our results showed fewer CTLs conjugated with target cells were activated in the stiff ECM mimic compared with the soft ECM mimic. Moreover, the lag time between contact and activation was longer in the stiffer environment, suggesting that the activated CTLs required longer time to recognize their target cells. In addition, we quantified phospho-ZAP70, a proximal readout of productive TCR triggering, and found higher matrix stiffness was associated with reduced phospho-ZAP70 intensity in CTLs conjugated with cognate antigen presenting APCs, supporting the conclusion that stiffness limits efficient TCR-proximal signaling and the persistence of signaling-competent synapses (*50*). Together, these findings indicate that stiff ECM conditions hinder CTLs' ability to recognize cognate target cells even upon contact, which could account for the reduced killing efficiency in stiff ECM mimic despite having similar count of CTL-target cell conjugates as the soft ECM mimic. Overall, our findings highlight that stiffer environment significantly impairs CTL motility, TCR recognition, immunological synapse formation, and overall cytotoxic efficacy, highlighting the critical role of biomechanical cues on regulating immune cell function. Furthermore, these findings provide a mechanistic explanation for how cancer cells evade antitumor response as increased tissue stiffness (a hallmark of solid tumors) disrupts CTL function (*51*).

In summary, we established a cytotoxicity assay using the RASTRUM 3D bioprinter to measure the antigen-specific CTL-killing efficiency in stiff and soft ECM mimics. The reductionist approach applied in this study is highly adaptable, is extensible to high-throughput assays, and can be further engineered to include other critical factors influencing tumor-specific T cell responses.

The mechanical properties of the ECM reciprocally influence stromal cell behavior, promoting immunosuppressive phenotypes. These cells secrete factors that further remodel the ECM and suppress T cell activity, creating a vicious cycle that perpetuates immune evasion and tumor progression (*52*). Expanding our system to integrate key cellular components, such as cancer-associated fibroblasts and macrophages, would provide deeper insights into their dynamics in a physiologically relevant 3D environment.

Although the work presented here shows a clear impact of ECM stiffness on CTL function on short time scales (<24 hours), it will be important in future studies to determine how prolonged exposure to stiffness and repeated stimulation shape CTL phenotype and transcriptional state. Recent work suggests that Osr2 can participate in longer-term T cell responses to mechanical cues (*19*); however, such transcriptional mechanoadaptation is mechanistically and temporally distinct from the acute functional regulation studied here. Extending this platform to multiday stimulation paradigms, together with comprehensive transcriptional and proteomic profiling of both

CTLs and target cells, will be valuable for connecting acute stiffness-dependent functional effects to longer-term adaptation.

In addition, the system can be leveraged to understand how ECM stiffness and porosity affect molecular transport properties because the diffusion of small molecules, such as cytokines and chemokines, is essential in regulating T cell function within the TME. Investigating how these physical properties shape immune responses could inform emerging therapeutic strategies aimed at disrupting the physical attributes of the TME. Approaches such as collagenase treatments, matrix-degrading nanoparticles, or inhibitors of ECM cross-linking enzymes are showing promise in preclinical studies, highlighting the critical interplay between ECM mechanics and immune function in tumors (*53*, *54*). Our platform offers a controlled environment to explore these strategies, inspiring immunotherapies that target ECM-driven immune suppression.

MATERIALS AND METHODS

Culture of target cells

Blue fluorescent protein (BFP)–expressing CHO-K1 (American Type Culture Collection, CCL-61) cells with or without the tetracycline repressor (CHO T-Rex cells; Invitrogen) and mouse OVA bound to H2Kb (T-Rex/OVA-H2Kb) were used as cognate antigen-presenting (OVA^+) and noncognate APCs (OVA^-), respectively (fig. S3, A and B). All CHO cell lines were cultured in Ham's F-12K medium (Gibco), supplemented with 10% fetal bovine serum (FBS; Bovogen), 100 mM L-glutamine (Gibco), and 1% penicillin-streptomycin (Gibco).

Isolation and ex vivo activation of OT-1 T cells

Mice experiments were conducted under protocols approved by the University of New South Wales (UNSW) Animal Care and Ethics Committees (approval numbers 17/104A and 19/148B). All mice were sourced from Australian BioResources (Mossvale, New South Wales) and housed under specific pathogen–free conditions within the Biological Resource Centre at UNSW. Male and female OT-1 [C57BL/6-Tg (TcraTcrb)] mice aged 6 to 12 weeks were used.

OT-1 $CD8^+$ T cells were isolated and cultured as previously described (fig. S2) (*33*). Briefly, splenocytes were obtained from OT-1 mouse spleens posteuthanasia, processed through a 40-μm strainer (Corning), and treated with Ammonium-Chloride-Potassium (ACK) lysing buffer (Gibco) to remove erythrocytes. Cells were cultured for 3 days in T cell medium (TCM) (RPMI 1640 supplemented with 10% FBS, 1% penicillin-streptomycin, 10 mM Hepes, 1% sodium pyruvate, 2 mM L-glutamine, and 50 μM β-mercaptoethanol) with interleukin-2 (IL-2) (100 ng/ml; BioLegend), lipopolysaccharide (0.03 μg/ml; Sigma-Aldrich), and OVA peptide (1 μg/ml; SIINFEKL) (Auspep). Cells were then collected, washed, resuspended in TCM with IL-2 to a density of 0.1×10^6 to 0.5×10^6/ml, transferred to a T25 flask, and incubated for 24 hours. The culture was used within a week while maintaining the cell density at 1×10^6/ml.

Bioprinting of cell-embedded ECM mimics

The RASTRUM 3D bioprinter and components of the ECM mimetic hydrogels (bioinks and bisthiol cross-linkers) were obtained from Inventia Life Science (ILS). To create the ECM mimetic hydrogels, we used a 20-kDa four-arm PEG maleimide bioink (F38) with a 2.64% w/v bisthiol cross-linker (F177) for soft gels and a 10-kDa four-arm PEG maleimide bioink (F119) with a 5.28% w/v bisthiol cross-linker (F178) for stiff gels. Medium was added after 5 min of printing. CTLs (1×10^6) were primed with the cross-linkers (200 μl), and target cells (1×10^6) were primed with a 200-μl bioink.

Stiffness measurement

The rheological properties of the ECM mimetic hydrogels were assessed using an Anton Paar MCR302 rheometer equipped with a 25-mm measuring plate. A 600-μl hydrogel sample was placed on the stage, and time-sweep measurements were recorded at 37°C with a frequency of 1 Hz and 0.1% strain over 2 hours. At least three replicates were performed for each hydrogel.

Cell viability

To assess the viability of each cell type after 3D bioprinting, cells with >95% viability before printing were used. CTLs and target cells were printed separately into wells of a flat-bottom, optical cover glass base 96-well microplate (Nunc). Following medium addition, cell viability was assessed at various time points using the LIVE/DEAD viability assay kit (Invitrogen). Images were acquired on the Operetta CLS Microscope equipped with a 5× air [numerical aperture (NA) of 0.16] objective and an incubator system (37°C, 5% CO_2). Image analysis was performed using Harmony Imaging and Analysis software (version 4.9, PerkinElmer Inc.).

T cell migration assay

CTLs (1×10^6) were stained with 0.5 μl of 1 mM CellTracker Deep Red (Invitrogen) and incubated in Dulbecco's phosphate-buffered saline (DPBS) for 10 to 15 min at 37°C. The stained cells were washed, resuspended in TCM, and incubated for 2 hours before bioprinting. The bisthiol cross-linker together with stained CTLs and the bioink with or without unstained OVA^+ target cells were printed using the RASTRUM 3D bioprinter into a glass bottom 96-well plate and incubated for another 2 hours before imaging. The migration of CTLs within the soft and stiff ECM mimetic hydrogels with and without the OVA^+ target cells was observed using a Zeiss Celldiscoverer 7 microscope equipped with a Plan-Apochromat 20× air (NA of 0.7) objective. 3D image stacks were acquired every 30 s, with a *z*-step size of 5 μm, covering a total *z*-depth of 200 μm and a total imaging duration of 1 hour per sample. The fluorescence signals were collected with excitation at 625 nm and 659- to 759-nm emission filter. Images were captured in both bright-field and fluorescence channels. During live cell imaging, the temperature and CO_2 level were kept at 37°C and 5%, respectively. The migration assay was performed with two biological repeats and with at least three experimental repeats.

Image analysis was performed using Imaris 9.9 (Bitplane), with cell tracking conducted using an autoregressive motion algorithm. The fluorescence intensity and positional coordinates at each time point for each cell were extracted from multiple imaging channels into CSV files. These data were subsequently combined using the Pandas library for further analysis. Cells touching the bottom of the well ($z < 10$ μm) were excluded from the dataset to ensure that only cells embedded within hydrogels were included in the analysis. The 3D average speed of a cell was calculated as the total distance travelled divided by the time interval between the first and last time points as described in Eq. 1

$$\text{3D average speed} = \frac{\sum_{i=0}^{n} \sqrt{\left(x_{i+1}-x_i\right)^2 + \left(y_{i+1}-y_i\right)^2 + \left(z_{i+1}-z_i\right)^2}}{t(n) - t(0)} \quad (1)$$

where x, y, and z refer to the position coordinates and t refers to time point with 0 and n, referring to the first and last time points, respectively.

Microscopy-based killing assay

The samples for T cell killing assay were prepared following a similar protocol as the migration assay with an additional step to stain the target cells. OVA^+ target cells (1×10^6) were stained with 0.5 μl of 1 mM CellTrace Violet (Invitrogen). After resting for 2 hours, stained CTLs mixed with the bisthiol cross-linker and stained target cells mixed with the bioink were 3D printed as described in the previous sections while maintaining an E:T ratio of 1:1. The 3D bioprinted samples were incubated for 24 hours before imaging. Thirty minutes before imaging, we added 80 μl of dead stain (2 mM ethidium homodimer-1) to each well.

The 3D live cell imaging was accomplished using Zeiss Celldiscoverer 7 900 (Plan-Apochromat 5×, NA of 0.35 air objective). The 3D image stacks were acquired with 3-μm z-step size and 300-μm total z-depth. The images were captured in bright-field and fluorescence channels. The fluorescence signals from each stain were collected as follows: for CellTracker Deep Red, excitation at 625 nm and 659- to 759-nm emission filter; for CellTrace Violet, excitation at 385 nm and 410- to 440-nm emission filter; and for ethidium homodimer-1, excitation at 511 nm and ≥600-nm emission filter. The beam splitter for ethidium homodimer-1 was a reflective thin film beam splitter (450, 538, and 610 nm) and for CellTracker Deep Red and CellTrace Violet was a reflective quartz beam splitter (405, 493, 575, and 653 nm) to avoid bleed-through between channels. During imaging, the temperature and CO_2 level were kept at 37°C and 5%, respectively. This killing assay was performed with two biological repeats and with at least three experimental repeats in each biological repeat.

The images were analyzed in Imaris 9.9 using spots module to detect and identify cells, as well as to determine cell death. The fluorescence intensity values of a cell from three channels were extracted from Imaris and merged to a Pandas DataFrame. The cell identity was verified by passing a threshold intensity value for CellTrace Violet or CellTracker Deep Red. The threshold value was determined by the built-in autothreshold algorithm in Imaris and visually inspecting that the detected cell with the lowest intensity value was a cell. The threshold was adjusted as necessary. The threshold value was distinct for each imaging experiment. A value higher than the threshold implies that the cell is either a target cell (CellTrace Violet) or a CTL (CellTracker Deep Red). Cells failing or passing both threshold values were labeled as unknown and were excluded from the dataset. Cells touching the bottom of the well ($z < 10$ μm) were also excluded from the dataset. Next, the identified cells were then classified as dead if they exceed the threshold value for ethidium homodimer-1. To calculate the killing efficiency of CTLs, we need to determine the viability of target cells. The viability of target cells in a sample was based on the difference between the total number of target cells and the number of targets cells that have ethidium homodimer-1 as described in Eq. 2

$$\text{Viability}\,[\%] = \frac{\text{target cell count} - \text{dead target cell count}}{\text{target cell count}} \times 100 \quad (2)$$

The killing efficiency was then calculated from the viability difference of the OVA^+ target cell in the presence and absence of CTLs. Killing efficiency was calculated using Eq. 3

$$\text{Killing efficiency}\,[\%] = \frac{\text{viability}_{\text{target cells only}} - \text{viability}_{\text{target cells coculture with T cells}}}{\text{viability}_{\text{target cells only}}} \times 100 \quad (3)$$

Flow cytometry–based killing assay

To induce expression of OVA-H2Kb on target cells, BFP CHO cells were cultured overnight with doxycycline (10 ng/ml; Clontech) before performing killing assays. A 1:1 mixture of target cells expressing OVA (OVA^+) and target cells without OVA (OVA^-) was used throughout the assay. For the 0:1 E:T ratio, target cells were bioprinted into a 96-well round-bottom microplate (Corning) without T cells. For other E:T ratios, CTLs were primed with cross-linkers, target cells were primed with bioinks, and both were bioprinted into the 96-well plates. TCM supplemented with IL-2 was added to each well, and the plate was incubated at 37°C for 24 hours.

After the 24-hour incubation, to recover cells for flow cytometry analysis, the 3D bioprinted ECM mimetic hydrogels were digested using RASTRUM Cell Retrieval Solution according to the manufacturer's instructions (F235, ILS). Briefly, each plate was washed with prewarmed DPBS, Cell Retrieval Solution was added to each well, and the plate was incubated at 37°C and 5% CO_2 for 5 min. Hydrogel dissolution was monitored using an epifluorescence inverted microscope. The plate was washed with prewarmed medium, and recovered cells were used for downstream flow cytometry analysis.

Before staining, all samples were washed with ice-cold fluorescence-activated cell sorting (FACS) buffer (2% FBS and 1 mM EDTA in sterile phosphate-buffered saline). Cells were blocked with 1:200 anti-mouse CD16/32 (TruStain FcX, BioLegend, clone 93) and stained for surface markers with 1:400 anti-mouse CD8 (BioLegend, clone 53-6.7) and 1:400 anti-SIINFEKL-H-2Kb (BioLegend, clone 25-D1.16) in FACS buffer for 15 to 20 min at 4°C in the dark. Cells were washed with ice-cold FACS buffer and resuspended in 100 μl of FACS buffer containing propidium iodide (2 μg/ml; Sigma-Aldrich) to exclude dead cells. Data collection was performed using a BD LSRFortessa Cell Analyzer with BD High Throughput Sampler, and postrecording analysis was carried out using FlowJo software v10.7 for Windows. The killing efficiency of OVA-expressing target cells was calculated using Eq. 4

$$\text{Killing}\,(\%) = \left(1 - \frac{\%\text{OVA+}}{\%\text{OVA−}}\right) \times 100 \quad (4)$$

The flow cytometry–based killing assay was performed with four biological repeats and with at least three experimental repeats each.

Time-lapse imaging of conjugate formation

The samples were prepared using the same protocol as the microscopy-based killing assay. The samples were imaged every 10 min for 12 hours using a Zeiss Celldiscoverer 7 microscope with Plan-Apochromat 5×, NA of 0.35 air objective. A total of 200-μm z-depth image stacks were acquired with 10-μm z-step size in bright-field and fluorescence channels. The fluorescence signals were collected following the same settings as the microscopy-based killing assay. During live cell imaging, the temperature and CO_2 level were kept at 37°C and 5%, respectively. The conjugate formation between CTLs and target cells was performed with two biological repeats and with at least three experimental repeats. The images were analyzed in Imaris 9.9. The cells from each channel were tracked using an autoregressive motion algorithm. The fluorescence intensity and position coordinates of each cell at each time point were extracted and processed in Python for further analysis.

For each time point, the cells were identified as CTLs or target cells following the same data analysis pipeline as described in the microscopy-based killing assay. From the position coordinates, the conjugates were identified by calculating the distance between CTLs and target cells

$$\text{Distance}_T = \sqrt{\left(x_{\text{target},T} - x_{\text{CTL},T}\right)^2 + \left(y_{\text{target},T} - y_{\text{CTL},T}\right)^2 + \left(z_{\text{target},T} - z_{\text{CTL},T}\right)^2} \quad (5)$$

where x, y, and z are the position coordinates and T refers to time.

A unique pair of CTL and target cell with distance of 12 μm or less between them are classified as one conjugate. The threshold 12 μm is based on the average sum of radii of a target cell and a CTL. The time points when a conjugate is detected, the target cell ID, and the T cell ID of the cells were extracted. From these details, number of conjugates, time of conjugation, time of release, and contact time were calculated.

Monitoring Ca^{2+} influx in conjugated CTLs

To study intracellular Ca^{2+} dynamics in effector T cells, the samples were prepared following the same protocol as the microscopy killing assay but without staining with ethidium homodimer-1. Instead, following bioprinting, cells embedded in soft and stiff ECM mimetic hydrogels were loaded with 3 μM Fluo-4 AM and Pluronic F-127 (Invitrogen) in imaging buffer (Hanks' balanced salt solution supplemented with 10 mM Hepes, 1 mM $CaCl_2$, 1 mM $MgCl_2$, and 1% FBS) and incubated for 30 min at 37°C in the dark. The samples were washed three times with medium and equilibrated at room temperature for 20 to 30 min before imaging. The calcium influxes in CTLs were monitored using an Operetta CLS confocal microscope (20×, NA of 1) equipped with a 37°C and 5% CO_2 incubation chamber. The 3D images (z-stack) were captured every 5 μm with a total height of 200 μm. The z-stack was imaged at frame intervals of 30 s for 1 hour. This assay was performed with two biological repeats and with three experimental repeats each.

Fluorescence changes of the Ca^{2+} indicator in CTLs conjugated with target cells were quantified using Imaris 9.9. The conjugates were identified as described in the microscopy-based killing assay. Then, the threshold intensity, denoting the presence of Ca^{2+} influx, was determined by Otsu's thresholding algorithm. The presence of Ca^{2+} influx indicates the activation of CTLs. The time when conjugation and activation occurred were also extracted. From these details, the relative number of activated CTLs conjugated with target cells and the lag time between conjugation and activation in soft and stiff ECM mimetic hydrogels were calculated and used as metrics to describe synapse quality.

Quantification of phospho-ZAP70 in conjugated CTLs

The samples were prepared following the same protocol as the microscopy killing assay but using a different fluorescent label for CTLs. CTLs (1×10^6) were instead stained with 0.5 μl of 1 mM CellTracker Green CMFDA (Invitrogen). The 3D bioprinted samples were incubated for 24 hours and were fixed with 4% paraformaldehyde at 4°C overnight, permeabilized with 0.1% Triton X-100 for 4 hours at room temperature, and incubated overnight at 4°C with anti-ZAP70 Phospho (Tyr^{319})/Syk Phospho (Tyr^{352}) monoclonal antibody (BioLegend, clone 1503310) conjugated with Alexa Fluor 647, diluted at 1:200 in DPBS. Between steps and after staining, the samples were washed with DPBS. The samples were then imaged using a Zeiss Cell Discovery 7 900 confocal microscope (Plan-Apochromat 20×, NA of 0.7 air objective) while immersed in clearing solution. The phospho-ZAP70 expression of CTLs conjugated with target cells was quantified using Imaris 9.9.

Statistical analysis

Image and data analysis are detailed in each method section. The data analysis flowchart, summarizing the numerical analysis, can also be found in fig. S5. Python 3.11.5 was used to further analyze the numerical data from the image analysis using the following libraries: numpy 1.24.3, pandas 2.0.3, matplotlib 3.7.2, seaborn 0.12.2, and SciPy 1.11.1. The resulting data were visualized, and statistical analyses were performed using GraphPad Prism software (version 10.2). Cell icons were created with BioRender, and schematics were prepared using Adobe Illustrator (version 29.1).

Supplementary Materials

This PDF file includes:

Supplementary Materials and Methods
Figs. S1 to S9
Legends for movies S1 and S2
Legends for datasets S1 to S4
Legend for data file S1

Other Supplementary Material for this manuscript includes the following:

Movies S1 and S2
Datasets S1 to S4
Data file S1

REFERENCES

1. M. R. Jenkins, G. M. Griffiths, The synapse and cytolytic machinery of cytotoxic T cells. *Curr. Opin. Immunol.* **22**, 308–313 (2010).
2. M. Faroudi, C. Utzny, M. Salio, V. Cerundolo, M. Guiraud, S. Muller, S. Valitutti, Lytic versus stimulatory synapse in cytotoxic T lymphocyte/target cell interaction: Manifestation of a dual activation threshold. *Proc. Natl. Acad. Sci. U.S.A.* **100**, 14145–14150 (2003).
3. J. Slaats, C. E. Dieteren, E. Wagena, L. Wolf, T. K. Raaijmakers, J. A. van der Laak, C. G. Figdor, B. Weigelin, P. Friedl, Metabolic screening of cytotoxic T cell effector function reveals the role of CRAC channels in regulating lethal hit delivery. *Cancer Immunol. Res.* **9**, 926–938 (2021).
4. A. Wiedemann, D. Depoil, M. Faroudi, S. Valitutti, Cytotoxic T lymphocytes kill multiple targets simultaneously via spatiotemporal uncoupling of lytic and stimulatory synapses. *Proc. Natl. Acad. Sci. U.S.A.* **103**, 10985–10990 (2006).
5. H. Mohammadi, E. Sahai, Mechanisms and impact of altered tumour mechanics. *Nat. Cell Biol.* **20**, 766–774 (2018).
6. K. R. Levental, H. Yu, L. Kass, J. N. Lakins, M. Egeblad, J. T. Erler, S. F. T. Fong, K. Csiszar, A. Giaccia, W. Weninger, M. Yamauchi, D. L. Gasser, V. M. Weaver, Matrix crosslinking forces tumor progression by enhancing integrin signaling. *Cell* **139**, 891–906 (2009).
7. M. F. Krummel, F. Bartumeus, A. Gerard, T cell migration, search strategies and mechanisms. *Nat. Rev. Immunol.* **16**, 193–201 (2016).
8. H. Salmon, K. Franciszkiewicz, D. Damotte, M. C. Dieu-Nosjean, P. Validire, A. Trautmann, F. Mami-Chouaib, E. Donnadieu, Matrix architecture defines the preferential localization and migration of T cells into the stroma of human lung tumors. *J. Clin. Invest.* **122**, 899–910 (2012).
9. K. Wolf, R. Müller, S. Borgmann, E.-B. Bröcker, P. Friedl, Amoeboid shape change and contact guidance: T-lymphocyte crawling through fibrillar collagen is independent of matrix remodeling by MMPs and other proteases. *Blood* **102**, 3262–3269 (2003).
10. X. Li, T. Gruosso, D. Zuo, A. Omeroglu, S. Meterissian, M. C. Guiot, A. Salazar, M. Park, H. Levine, Infiltration of $CD8^+$ T cells into tumor cell clusters in triple-negative breast cancer. *Proc. Natl. Acad. Sci. U.S.A.* **116**, 3678–3687 (2019).
11. R. R. Ji, S. D. Chasalow, L. Wang, O. Hamid, H. Schmidt, J. Cogswell, S. Alaparthy, D. Berman, M. Jure-Kunkel, N. O. Siemers, J. R. Jackson, V. Shahabi, An immune-active tumor microenvironment favors clinical response to ipilimumab. *Cancer Immunol. Immunother.* **61**, 1019–1031 (2012).
12. J. L. Carstens, P. Correa de Sampaio, D. Yang, S. Barua, H. Wang, A. Rao, J. P. Allison, V. S. LeBleu, R. Kalluri, Spatial computation of intratumoral T cells correlates with survival of patients with pancreatic cancer. *Nat. Commun.* **8**, 15095 (2017).

13. H. Simsek, E. Klotzsch, The solid tumor microenvironment-breaking the barrier for T cells: How the solid tumor microenvironment influences T cells. *Bioessays* **44**, e2100285 (2022).
14. S. M. Albelda, CAR T cell therapy for patients with solid tumours: Key lessons to learn and unlearn. *Nat. Rev. Clin. Oncol.* **21**, 47–66 (2024).
15. A. J. McKenzie, S. R. Hicks, K. V. Svec, H. Naughton, Z. L. Edmunds, A. K. Howe, The mechanical microenvironment regulates ovarian cancer cell morphology, migration, and spheroid disaggregation. *Sci. Rep.* **8**, 7228 (2018).
16. A. Nicolas-Boluda, J. Vaquero, L. Vimeux, T. Guilbert, S. Barrin, C. Kantari-Mimoun, M. Ponzo, G. Renault, P. Deptula, K. Pogoda, R. Bucki, I. Cascone, J. Courty, L. Fouassier, F. Gazeau, E. Donnadieu, Tumor stiffening reversion through collagen crosslinking inhibition improves T cell migration and anti-PD-1 treatment. *eLife* **10**, e58688 (2021).
17. Z. Mai, Y. Lin, P. Lin, X. Zhao, L. Cui, Modulating extracellular matrix stiffness: A strategic approach to boost cancer immunotherapy. *Cell Death Dis.* **15**, 307 (2024).
18. L. H. Porter, J. J. Zhu, N. L. Lister, S. G. Harrison, S. Keerthikumar, D. L. Goode, R. Q. Urban, D. J. Byrne, A. Azad, I. Vela, M. S. Hofman, P. J. Neeson, P. K. Darcy, J. A. Trapani, R. A. Taylor, G. P. Risbridger, Low-dose carboplatin modifies the tumor microenvironment to augment CAR T cell efficacy in human prostate cancer models. *Nat. Commun.* **14**, 5346 (2023).
19. J. Zhang, J. Li, Y. Hou, Y. Lin, H. Zhao, Y. Shi, K. Chen, C. Nian, J. Tang, L. Pan, Y. Xing, H. Gao, B. Yang, Z. Song, Y. Cheng, Y. Liu, M. Sun, Y. Linghu, J. Li, H. Huang, Z. Lai, Z. Zhou, Z. Li, X. Sun, Q. Chen, D. Su, W. Li, Z. Peng, P. Liu, W. Chen, H. Huang, Y. Chen, B. Xiao, L. Ye, L. Chen, D. Zhou, Osr2 functions as a biomechanical checkpoint to aggravate $CD8^+$ T cell exhaustion in tumor. *Cell* **187**, 3409–3426.e24 (2024).
20. K. P. Meng, F. S. Majedi, T. J. Thauland, M. J. Butte, Mechanosensing through YAP controls T cell activation and metabolism. *J. Exp. Med.* **217**, e20200053 (2020).
21. P. Mu, S. Zhou, T. Lv, F. Xia, L. Shen, J. Wan, Y. Wang, H. Zhang, S. Cai, J. Peng, G. Hua, Z. Zhang, Newly developed 3D in vitro models to study tumor-immune interaction. *J. Exp. Clin. Cancer Res.* **42**, 81 (2023).
22. E. A. Aisenbrey, W. L. Murphy, Synthetic alternatives to Matrigel. *Nat. Rev. Mater.* **5**, 539–551 (2020).
23. E. Y. Du, H. T. K. Duong, M. A. K. Tolentino, J. L. Houng, P. Suwannakot, K. C. Tjandra, D. H. T. Nguyen, R. D. Tilley, J. J. Gooding, Ionically crosslinked biohybrid gelatin-based hydrogels for 3D cell culture. *Macromol. Res.* **33**, 921–931 (2025).
24. M. Jung, J. N. Skhinas, E. Y. Du, M. A. K. Tolentino, R. H. Utama, M. Engel, A. Volkerling, A. Sexton, A. P. O'Mahony, J. C. C. Ribeiro, J. J. Gooding, M. Kavallaris, A high-throughput 3D bioprinted cancer cell migration and invasion model with versatile and broad biological applicability. *Biomater. Sci.* **10**, 5876–5887 (2022).
25. P. Suwannakot, L. Zhu, M. A. K. Tolentino, E. Y. Du, A. Sexton, S. Myers, J. J. Gooding, Electrostatically cross-linked bioinks for jetting-based bioprinting of 3D cell cultures. *ACS Appl. Bio Mater.* **7**, 269–283 (2024).
26. E. Pérez Del Río, F. Santos, X. R. Rodriguez, M. Martínez-Miguel, R. Roca-Pinilla, A. Arís, E. Garcia-Fruitós, J. Veciana, J. P. Spatz, I. Ratera, J. Guasch, CCL21-loaded 3D hydrogels for T cell expansion and differentiation. *Biomaterials* **259**, 120313 (2020).
27. H. H. Hwang, S. You, X. Ma, L. Kwe, G. Victorine, N. Lawrence, X. Wan, H. Shen, W. Zhu, S. Chen, High throughput direct 3D bioprinting in multiwell plates. *Biofabrication* **13**, 025007 (2021).
28. R. H. Utama, L. Atapattu, A. P. O'Mahony, C. M. Fife, J. Baek, T. Allard, K. J. O'Mahony, J. C. C. Ribeiro, K. Gaus, M. Kavallaris, J. J. Gooding, A 3D bioprinter specifically designed for the high-throughput production of matrix-embedded multicellular spheroids. *iScience* **23**, 101621 (2020).
29. C. Mazzaglia, Y. Y. Shery Huang, J. D. Shields, Advancing tumor microenvironment and lymphoid tissue research through 3D bioprinting and biofabrication. *Adv. Drug Deliv. Rev.* **217**, 115485 (2025).
30. J. P. Joseph, S. B. Gugulothu, D. Nandi, K. Chatterjee, Mechanical properties affect primary T cell activation in 3D bioprinted hydrogels. *ACS Macro Lett.* **12**, 1085–1093 (2023).
31. A. Purwada, S. B. Shah, W. Béguelin, A. August, A. M. Melnick, A. Singh, Ex vivo synthetic immune tissues with T cell signals for differentiating antigen-specific, high affinity germinal center B cells. *Biomaterials* **198**, 27–36 (2019).
32. B. Delalat, F. Harding, B. Gundsambuu, E. M. De-Juan-Pardo, F. M. Wunner, M. L. Wille, M. Jasieniak, K. A. L. Malatesta, H. J. Griesser, A. Simula, D. W. Hutmacher, N. H. Voelcker, S. C. Barry, 3D printed lattices as an activation and expansion platform for T cell therapy. *Biomaterials* **140**, 58–68 (2017).
33. M. A. K. Tolentino, M. H. Seyedzadeh, N. G. Peres, E. Y. Du, L. Zhu, K. Gaus, J. Goyette, J. J. Gooding, Polyethylene glycol-based hydrogel as a 3D extracellular matrix mimic for cytotoxic T lymphocytes. *J. Biomed. Mater. Res. A* **113**, e37811 (2025).
34. R. H. Utama, V. T. G. Tan, K. C. Tjandra, A. Sexton, D. H. T. Nguyen, A. P. O'Mahony, E. Y. Du, P. Tian, J. C. C. Ribeiro, M. Kavallaris, J. J. Gooding, A covalently crosslinked ink for multimaterials drop-on-demand 3D bioprinting of 3D cell cultures. *Macromol. Biosci.* **21**, e2100125 (2021).
35. M. A. K. Tolentino, E. Y. Du, G. Silvani, E. Pandzic, K. A. Kilian, J. J. Gooding, Decoding hydrogel porosity: Advancing the structural analysis of hydrogels for biomedical applications. *Adv. Healthc. Mater.* **14**, e2500658 (2025).
36. E. Y. Du, M. Jung, J. Skhinas, M. A. K. Tolentino, J. Noy, N. Jamshidi, J. L. Houng, K. C. Tjandra, M. Engel, R. Utama, R. D. Tilley, M. Kavallaris, J. J. Gooding, 3D bioprintable hydrogel with tunable stiffness for exploring cells encapsulated in matrices of differing stiffnesses. *ACS Appl. Bio Mater.* **6**, 4603–4612 (2023).
37. E. D. Tabdanov, N. J. Rodríguez-Merced, A. X. Cartagena-Rivera, V. V. Puram, M. K. Callaway, E. A. Ensminger, E. J. Pomeroy, K. Yamamoto, W. S. Lahr, B. R. Webber, B. S. Moriarity, A. S. Zhovmer, P. P. Provenzano, Engineering T cells to enhance 3D migration through structurally and mechanically complex tumor microenvironments. *Nat. Commun.* **12**, 2815 (2021).
38. R. Zhao, X. Zhou, E. S. Khan, D. Alansary, K. S. Friedmann, W. Yang, E. C. Schwarz, A. Del Campo, M. Hoth, B. Qu, Targeting the microtubule-network rescues CTL killing efficiency in dense 3D matrices. *Front. Immunol.* **12**, 729820 (2021).
39. B. Weigelin, A. T. den Boer, E. Wagena, K. Broen, H. Dolstra, R. J. de Boer, C. G. Figdor, J. Textor, P. Friedl, Cytotoxic T cells are able to efficiently eliminate cancer cells by additive cytotoxicity. *Nat. Commun.* **12**, 5217 (2021).
40. Z. Li, G. S. Shaw, Role of calcium-sensor proteins in cell membrane repair. *Biosci. Rep.* **43**, BSR20220765 (2023).
41. M. Trebak, J. P. Kinet, Calcium signalling in T cells. *Nat. Rev. Immunol.* **19**, 154–169 (2019).
42. A. Maul-Pavicic, S. C. C. Chiang, A. Rensing-Ehl, B. Jessen, C. Fauriat, S. M. Wood, S. Sjöqvist, M. Hufnagel, I. Schulze, T. Bass, W. W. Schamel, S. Fuchs, H. Pircher, C.-A. McCarl, K. Mikoshiba, K. Schwarz, S. Feske, Y. T. Bryceson, S. Ehl, ORAI1-mediated calcium influx is required for human cytotoxic lymphocyte degranulation and target cell lysis. *Proc. Natl. Acad. Sci. U.S.A.* **108**, 3324–3329 (2011).
43. N. Otsu, A threshold selection method from gray-level histograms. *IEEE Trans. Syst. Man Cybern.* **9**, 62–66 (1979).
44. Z. Jin, X. Li, X. Zhang, P. DeSousa, T. Xu, A. Wu, Engineering the fate and function of human T-cells via 3D bioprinting. *Biofabrication* **13**, 035016 (2021).
45. J. W. Hickey, Y. Dong, J. W. Chung, S. F. Salathe, H. C. Pruitt, X. Li, C. Chang, A. K. Fraser, C. A. Bessell, A. J. Ewald, S. Gerecht, H.-Q. Mao, J. P. Schneck, Engineering an artificial T-cell stimulating matrix for immunotherapy. *Adv. Mater.* **31**, e1807359 (2019).
46. D. E. Kuczek, A. M. H. Larsen, M. L. Thorseth, M. Carretta, A. Kalvisa, M. S. Siersbæk, A. M. C. Simões, A. Roslind, L. H. Engelholm, E. Noessner, M. Donia, I. M. Svane, P. T. Straten, L. Grøntved, D. H. Madsen, Collagen density regulates the activity of tumor-infiltrating T cells. *J. Immunother. Cancer* **7**, 68 (2019).
47. E. Pérez Del Río, M. Martinez Miguel, J. Veciana, I. Ratera, J. Guasch, Artificial 3D culture systems for T cell expansion. *Omega* **3**, 5273–5280 (2018).
48. M. Jung, S. Ghamrawi, E. Y. Du, J. J. Gooding, M. Kavallaris, Advances in 3D bioprinting for cancer biology and precision medicine: From matrix design to application. *Adv. Healthc. Mater.* **11**, e2200690 (2022).
49. S. Budhu, J. D. Loike, A. Pandolfi, S. Han, G. Catalano, A. Constantinescu, R. Clynes, S. C. Silverstein, $CD8^+$ T cell concentration determines their efficiency in killing cognate antigen-expressing syngeneic mammalian cells in vitro and in mouse tissues. *J. Exp. Med.* **207**, 223–235 (2010).
50. J. Goyette, D. Depoil, Z. Yang, S. A. Isaacson, J. Allard, P. A. van der Merwe, K. Gaus, M. L. Dustin, O. Dushek, Dephosphorylation accelerates the dissociation of ZAP70 from the T cell receptor. *Proc. Natl. Acad. Sci. U.S.A.* **119**, e2116815119 (2022).
51. J. J. F. Sleeboom, G. S. van Tienderen, K. Schenke-Layland, L. J. W. van der Laan, A. A. Khalil, M. M. A. Verstegen, The extracellular matrix as hallmark of cancer and metastasis: From biomechanics to therapeutic targets. *Sci. Transl. Med.* **16**, eadg3840 (2024).
52. D. H. Munn, V. Bronte, Immune suppressive mechanisms in the tumor microenvironment. *Curr. Opin. Immunol.* **39**, 1–6 (2016).
53. H. Y. Huang, L. Q. Chen, W. Sun, H. H. Du, S. Dong, A. M. Q. Ahmed, D. Cao, J. H. Cui, Y. Zhang, Q. R. Cao, Collagenase IV and clusterin-modified polycaprolactone-polyethylene glycol nanoparticles for penetrating dense tumor tissues. *Theranostics* **11**, 906–924 (2021).
54. J. Huang, L. Zhang, D. Wan, L. Zhou, S. Zheng, S. Lin, Y. Qiao, Extracellular matrix and its therapeutic potential for cancer treatment. *Signal Transduct. Target. Ther.* **6**, 153 (2021).

Acknowledgments: We thank the funding support from the National Health and Medical Research Council (NHMRC) Investigator (GNT1196648 to J.J.G.), NHMRC Synergy Grant (GNT2019056 to J.J.G.), and NHMRC Ideas Grants (GNT2021307 and GNT1183588 to J.G.). We would like to acknowledge the support and help from the staff of Katharina Gaus Light Microscopy Facility (KGLMF) and the Flow Cytometry Facility at the Mark Wainwright Analytical Centre, UNSW, specifically E. J. Beves and E. Pandzic. **Funding:** This work was supported by the National Health and Medical Research Council (NHMRC) Investigator (GNT1196648 to J.J.G.), NHMRC Synergy Grant (GNT2019056 to J.J.G.), and NHMRC Ideas Grants (GNT2021307 and

GNT1183588 to J.G.). **Author contributions:** Conceptualization: M.H.S., M.A.K.T., K.G., J.G., and J.J.G. Methodology: M.H.S., M.A.K.T., N.G.P., F.B.-T., G.M.N.J., K.A.K., J.G., and J.J.G. Investigation: M.H.S., M.A.K.T., N.G.P., and E.Y.D. Data curation: M.H.S., M.A.K.T., and N.G.P. Software: M.A.K.T. Analysis: M.H.S., M.A.K.T., N.G.P., F.B.-T., and G.M.N.J. Visualization: M.H.S. and M.A.K.T. Project administration: K.G., J.G., and J.J.G. Funding acquisition: J.G. and J.J.G. Supervision: K.G., J.G., and J.J.G. Writing—original draft: M.H.S. and M.A.K.T. Writing—review and editing: K.A.K., J.G., and J.J.G. **Competing interests:** The authors declare that they have no competing interests. **Data, code, and materials availability:** All data and code needed to evaluate and reproduce the results in the paper are present in the paper and/or the Supplementary Materials. Custom Python scripts used to identify cell conjugates are provided as data file S1. This study did not generate new materials.

Submitted 16 April 2025
Accepted 18 June 2026
Published 31 July 2026
10.1126/sciadv.ady2299